Collision-Resilient Passive Deformable Quadrotors for Exploration, Mapping and Swift Navigation

*Karishma Patnaik Aravind Adhith Pandian Saravanakumaran Wenlong Zhang**

Ira A. Fulton Schools of Engineering, Arizona State University, Mesa, AZ, 85212, USA.
email: kpatnaik@asu.edu, apandia1@asu.edu, wenlong.zhang@asu.edu

Keywords: *morphing drones, contact-based exploration, agile navigation, external force estimation*

In this article, we introduce XPLORER, a passive deformable quadrotor optimized for performing contact-rich tasks by utilizing collision-induced deformation. We present a novel external force estimation technique, and advanced planning and control algorithms that exploit the compliant nature of XPLORER's chassis. These algorithms enable three distinct flight behaviors: static-wrench application, where XPLORER can exert desired forces and torque on surfaces for precise manipulation; disturbance rejection, wherein the quadrotor actively mitigates external forces and yaw disturbances to maintain its intended trajectory; and yielding to disturbance, enabling XPLORER to dynamically adapt its position and orientation to evade undesired forces, ensuring stable flight amidst unpredictable environmental factors. Leveraging these behaviors, we develop innovative mission strategies including *tactile-traversal*, *tactile-turning*, and *collide-to-brake* for contact-based exploration of unknown areas, contact-based mapping and swift navigation. Through experimental validation, we demonstrate the effectiveness of these strategies in enabling efficient exploration and rapid navigation in unknown environments, leveraging collisions as a means for feedback and control. This study contributes to the growing field of aerial robotics by showcasing the potential of passive deformable quadrotors for versatile and robust interaction tasks in real-world scenarios.

1 Introduction

Unmanned aerial vehicles (UAVs) have seen their missions expanding from surveillance to aerial manipulation and physical interaction tasks such as pick and place, grasping, perching, and pushing/pulling [1–3]. Conventional methods try to accomplish these missions by augmenting UAVs with additional protective gears, graspers, and manipulators to perform the various tasks, coupled with appropriate task-specific control algorithms [4–6]. While extensive research with such augmented platforms have shown great promise, researchers have also discovered that reconfigurability and mechanical intelligence of a UAV chassis can enhance endurance, beget versatility, improve flight efficiency, and enable safe interaction, all at once [7–9]. Accordingly, various morphing quadrotors have been designed and evaluated for achieving folding, multi-media locomotion and grasping [10–12].
A majority of such morphing UAVs, however, have active actuation mechanisms for initiating a change in their morphology, classified as *active* morphing aerial vehicle. In contrast, when the aerial vehicle reacts to external physical forces and undergoes a change in morphology, we call it a *passive* morphing aerial vehicle [9]. For such vehicles, collision energies are harnessed to initiate deformation using various materials and structures such as springs, foldable origami, and inflatable textiles leading to fast recovery post collisions [13–16]. This article aims at developing algorithm frameworks for such collision-resilient quadrotors to perform aerial-physical interaction tasks in real-world scenarios.

1.1 Related Literature

Critical to any robot-environment physical interaction tasks is the external wrench estimation algorithm which is used to design the interaction controllers [17]. Consequently, external wrench estimation and interaction control have been extensively investigated in the context of aerial robots and aerial manipulation [18–20]. The goal of this article is to tailor these concepts for implementation on passive deforming quadrotors to push objects as well as explore and map the environments. Furthermore, due to the collision-resilient feature, we aim to leverage collisions for demonstrating collision-inclusive agile flight behaviors, such as minimum time flights by deliberately colliding and stopping. Accordingly, a brief overview of related work on wrench estimation, contact-based inspection, contact-based/collision-inclusive navigation, and map generation is given in the sections below.

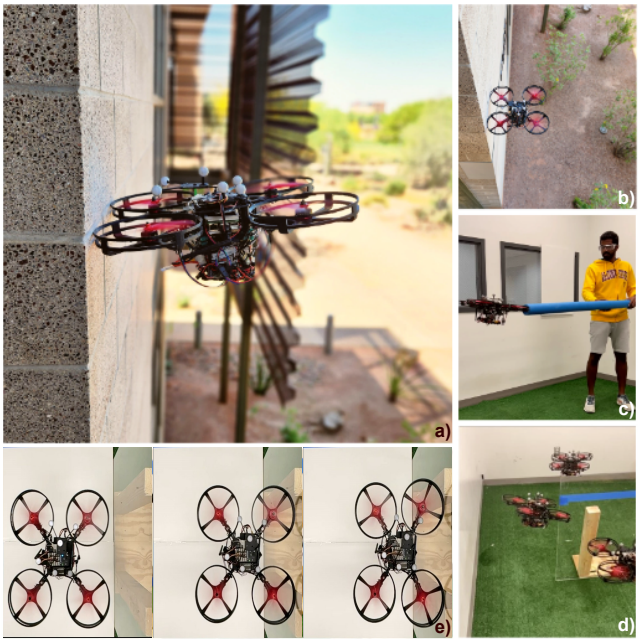

Figure 1: An overview of XPLORER performing various aerial-physical interaction tasks. (a) & (b) Overall vision of this work for deployment in outdoor surveillance missions. (c) Safe interaction policies implemented to enable aerial-human interaction, (d) Collide-to-decelerate maneuver, and (e) A sequence of slow-motion snapshots to highlight the deformation of XPLORER's chassis for establishing smooth contacts.

1.1.1 External Wrench Estimation

There are generally two approaches for estimating the external wrenches: the first method is to augment the aerial vehicle with sensors such as the force-torque sensors and the second method is to estimate the wrench using onboard sensors. The first method increases the total weight of the aerial vehicle platform and adversely affects flight time [21, 22]. For the second method, researchers have developed algorithms based on momentum-based [23, 24] and acceleration-based [19, 25] wrench estimators which rely on only the available onboard sensors such as inertial measurement units (IMUs). To improve the estimation in presence of sensor noise, a Kalman-filter based approach for wrench estimation was proposed in [26]. Authors of [27] presented significantly more accurate wrench estimates by combining the momentum-based and acceleration-based approaches. For this work, we aim at improving the acceleration-based wrench estimation algorithm by utilizing proprioceptive information about the vehicle's current morphology and generate an accurate wrench estimate.

1.1.2 Applications of the External Wrench

Static Force Application and Contact-based Inspection: With the knowledge of the external wrench, UAVs can now be pursued for performing contact-based tasks such as non-destructive testing, vibration analysis and leak identification which require a desired wrench to be applied onto a surface in an attempt to reduce safety risks to human workers [28, 29]. Successful applications are demonstrated in [30–32] where the researchers employ conventional rigid multirotor UAVs augmented with external protective gears or end-effectors for performing these contact-rich tasks. One potential issue using rigid-chassis UAVs for such tasks is the presence of unknown surface features which can introduce discontinuities and adversely affect the stability by inducing large changes in the UAV dynamics and states [33]. In this context, we propose to employ soft deformable quadrotors to establish smooth contacts and simplify the contact laws [34].

Contact-based Navigation: The collision-resilient designs hold a strong potential for a paradigm shift from obstacle detection for localization and mapping [35–39] to tactile-based exploration schemes, also called contact-based navigation. This also is an effective way to reduce weight from the additional sen-

sors that can adversely affect flight time. Contact-based navigation has been successfully implemented by researchers for various applications. Tactile-sensors [40, 41] or inertial measurement units (IMUs) can be successfully used to detect collisions in this case [18, 27, 42]. Then, the motion planner can replan online trajectories by considering these obstacles. A contact-based navigation planner was proposed in [43] consisting of two modes, sliding and flying cartwheel. The UAV switches to the cartwheel motion when there are no feasible trajectory for sliding mode or if the UAV gets stuck to some map inconsistencies. The authors do state that the flying cartwheel mode has the risk of high collision forces and demanding for robust state estimation. Authors of [41] utilized vision systems to navigate manhole-sized tubes along with flaps to sense contacts. In [44], authors used point cloud information of the environment to compute the trajectory for navigation. In [45] collisions were exploited for path planning using sampling-based methods. The common factor among all these works is that complete knowledge of the map of the environment is known a-priori and they utilize it to compute the trajectory. Navigation in an unknown environment is still nascent and remains an open problem. In [40], the authors proposed a random exploration algorithm, where the vehicle behaves like a bee and starts moving in the direction away from the obstacle. One limitation of this methodology is that with random exploration the coverage rate is not optimal and it is difficult to reproduce the results. Notably, existing work has not leveraged deformable designs to improve flight agility and achieve minimum flight time maneuvers which is one of the goals of our work.

Mapping: Exploration and mapping of an environment are synergistic actions and foundations for simultaneous localization and mapping (SLAM). This map generated can be used for trajectory generation by the same vehicle or for other autonomous vehicles. Conventionally, mapping an environment is performed by using cameras and Structure from Motion (SfM) technique [46]. SfM is the process of recreating a 3D structure from a series of images captured from different angles. Authors of [47] proposed an algorithm that used data from Light Detection And Ranging (LiDAR) and a stereo camera to generate a high-resolution map of the environment. As research progressed, real-time map generation was achieved using SLAM algorithms. [48, 49] used a monocular camera to carry out feature recognition and extraction to generate the map and also to localize the UAV in the map. Similarly, SLAM was implemented using a 2-axis LiDAR as shown in [50]. Research carried out in [51] used the combination of cameras, LiDAR, IMU, and encoders to generate a highly precise map of the environment. Another novel map generation methodology was presented in [27] where collision detection and localization were used to insert obstacle blocks into the point cloud map. However, the inserted block dimension is constant and does not accurately represent the dimensions of the obstacle, leading to limited online applications.

1.2 Contributions of Present Work

Existing work on the mechanically compliant, passive deformable quadrotors focuses on improving collision resilience [9, 52]; they have not been investigated to perform contact-based inspection which requires the UAV to maintain continuous contact with the desired object [15, 53]. Our previous work introduces various mechanical designs to obtain 2D and 3D collision resilience which looks beyond collision resilience and proposes harnessing the collision energies to undergo deformation for squeeze-and-fly and perching tasks [13, 54]. Furthermore, in [15], we proposed a recovery controller to stabilize the vehicle after collision by establishing that the post-collision velocities for the passive deformable quadrotors are low and hence the pre-collision velocity can be used to generate a desired position setpoint in the opposite direction of approach. Researchers in [14] presented another collision-tolerant vehicle with a recovery controller which leveraged collision characterization to generate a desired position setpoint. Controlled collision was further exploited in [55] to demonstrate narrow gap traversal with a soft foldable frame. However, this article aims to explore further benefits of these novel passive reconfigurable quadrotors for performing exhaustive contact-rich tasks such as exploration, navigation and mapping. The advantage of having a deformable chassis makes passive reconfigurable UAVs as ideal candidates to make, break or sustain contacts and apply desired contact forces without exhaustive hybrid control strategies.
The main contributions of the article are to explore the benefits of compliant and collision-tolerant UAVs

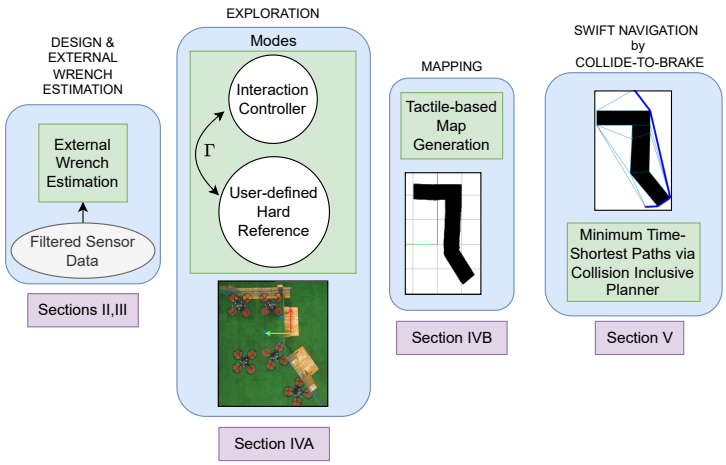

Figure 2: Our article aims to explore the benefits of passive deformable collision tolerant UAVs for exploration, mapping and navigation of unknown environments by exploiting collisions and contacts.

for exploration and mapping of unknown environments and to perform agile navigation by exploiting collisions and contacts. Towards this, we present the following significant contributions:

1. Development of a novel external force estimation algorithm: We propose an innovative algorithm to improve the accuracy and efficiency of estimating external forces acting on the quadrotor, particularly those resulting from contacts made at the arms. Through comprehensive validation in both free flight and contact scenarios, we demonstrate the superior performance of our algorithm compared to conventional methods that solely rely on center of mass information.

2. Introduction of tactile navigation for exploring unknown flight spaces: Leveraging the external force estimates, we devise two autonomous flight navigation modes - *Tactile-traversal* and *Tactile-turning* that utilize external force and yaw rate information to navigate through unexplored areas effectively. Our exploration strategy for collision resilient UAVs such as XPLORER, achieves optimal coverage of flight spaces as demonstrated through extensive simulations and real-life experiments, showcasing its practicality and efficacy.

3. Generation of maps of previously unknown environments through contact-based exploration: We propose a point-cloud-based methodology to create accurate maps of unknown spaces, achieving a validation accuracy of 96.72%. This enables the quadrotor to generate detailed maps of environments it encounters during exploration missions, contributing to improved situational awareness and mission planning.

4. Introduction of novel collide-to-brake maneuvers to reach goal locations in minimum time: By leveraging collision energy dissipation, we demonstrate the potential to minimize the overall time required for the quadrotor to reach designated goal locations as compared to collision avoiding braking. This innovative approach harnesses collisions as a means of deceleration leading to optimized trajectories. These maneuvers cannot be performed by a rigid quadrotor due to the high intensity of shock endured by the chassis leading to damage upon repeated collisions.

Figure 1 showcases our compliant and passive deformable quadrotor, XPLORER, engaged in various contact-rich tasks, while Figure 2 provides an overview of the article. The paper is structured as follows: Section 2 provides an overview of the design and low-level control of the aerial vehicle, XPLORER. In Section 3, we introduce the novel external force estimation algorithm tailored for XPLORER's unique design. Section 4 elaborates on the three contact-based missions, with subsections 4.1 and 4.2 focusing on exploration and tactile-based mapping missions, respectively, while section 4.3 details collision-to-brake missions for waypoint tracking. Section 5 presents the results of the proposed algorithms in real-world implementations. Finally, Section 6 concludes the article and discusses potential avenues for future research.

Table 1: Nomenclature

Symbol	Definition
$\boldsymbol{x} \in \mathbb{R}^3$	3D position of the system
$\boldsymbol{v} \in \mathbb{R}^3$	3D translational velocity of the system
$\boldsymbol{R} \in \mathbb{R}^{3\times3}$	rotation matrix
$\boldsymbol{H} \in \mathbb{R}^{3\times3}$	inertia matrix of system, assumed constant
$\mathcal{O}_w$	vehicle geometric center
${}_w\mathcal{F} = \{\boldsymbol{e_1}, \boldsymbol{e_2}, \boldsymbol{e_3}\}$	inertial frame
${}_b\mathcal{F} = \{\boldsymbol{b_1}, \boldsymbol{b_2}, \boldsymbol{b_3}\}$	body fixed frame, with $\mathcal{O}_w$ fixed at the geometric center of the frame
$\theta_i \in \mathbb{R}$	angle made by the i^{th} arm with the b_2 axis. This follows the right-hand rule
${}_{(\cdot)}(\bullet)$	denotes the quantity $(\bullet)$ in the $(\cdot)$ frame
${}_{a_i}\mathcal{F} = \{\boldsymbol{a_1^i}, \boldsymbol{a_2^i}\}$	i^{th} arm frame with $a_j^i \ \forall j = 1, 2$ denoting the basis vectors for the i^{th} frame
$k \in \mathbb{R}, b \in \mathbb{R}$	stiffness and damping coefficient for the arm dynamics
$\hat{\boldsymbol{\delta}}_a^i \in \mathbb{R}^6$	estimated wrench from the spring action at i^{th} arm
$l \in \mathbb{R}$	lever arm to obtain contact force from the torque estimate
$\hat{\delta}_{f_a}^i \in \mathbb{R}^3$	estimated net force at the i^{th} arm
$\boldsymbol{C}_n \in \mathbb{R}^4$	contact normal to the obstacle
$\lambda \in \mathbb{R}$	current move direction of the vehicle
$d_{step} \in \mathbb{R}$	distance to move for each step
$\dot{\psi}_0 \in \mathbb{R}$	yaw rate threshold
$\dot{\psi}_c \in \mathbb{R}$	*Tactile-turning* yaw rate
$\delta_0 \in \mathbb{R}$	force threshold for exploration & *Tactile-traversal*
$\delta_{\psi_0} \in \mathbb{R}$	force threshold for *Tactile-turning*
$f_{des} \in \mathbb{R}$	force to be applied on the obstacle
$\delta_{map} \in \mathbb{R}$	force threshold for mapping
$\Upsilon \in \mathbb{R}$	indicates if a contact is made by using the arm angle deviation information

2 System Description

A brief overview of the system, XPLORER, is given in the following subsections for the design and the low-level control. For the remainder of the article, we follow the standard notation for variables: lowercase, non-bold for scalars; lowercase, bold for vectors; uppercase, bold for matrices.

2.1 Design of XPLORER

In this work, we use a modified version of the passive foldable aerial robot, SQUEEZE, presented in our previous work [13]. Built on a similar idea, XPLORER (shown in Fig. 1) also has four deformable arms as part of its morphing chassis, but it does not retain the complete arm rotation to 90^o like its predecessor. The springs chosen for the current version are also stiffer than our previous design to ensure that the collision-induced deformation is induced in a smaller range. The free rotation is limited to 30^o due to the preferred in-plane placement of the arms unlike in SQUEEZE. This design choice was made for two specific reasons, with the first being that we wanted to lower the height of the center of mass (CoM) from our previous design to prevent toppling when making contact with the environment. This is shown in Fig. 1(e) where the deformation of the chassis easily allows large forces around 1N to be exerted on the environment without pitching into the wall, unlike the rigid conventional chassis. Secondly, we need to ensure that the vehicle will not get stuck in corner cases during exploration and hence redesigned the propeller guards, so a maximum of 30^o of free rotation was obtained as a result. Accordingly, since the scope of this article is to explore contact-based tasks and not to showcase squeeze and fly abilities, we limit the linear velocities to 4 m/s such that collisions which result in more than 30^o arm deformation are avoided. Each arm has a sensor attached to it to measure its relative orientation with respect to the body, which will be later used for external wrench estimation.

2.2 Control Framework

In this section, we describe the complete control framework for XPLORER. The control block diagram is shown in Fig. 3. The coordinate frame definitions and symbols used are described in Table 1 and are shown in Fig. 4. Each arm frame, ${}_{a_i}\mathcal{F}$, is located at a distance r_i from the geometric center ($\mathcal{O}_w$) of the frame. The body frame, ${}_b\mathcal{F}$ denotes the body-fixed frame $\{b_1, b_2, b_3\}$ located at $\mathcal{O}_w$ while ${}_w\mathcal{F}$ denotes the inertial frame $\{e_1, e_2, e_3\}$.
With $f \in \mathbb{R}$ denoting the total thrust along the $-b_3$ axis and $\boldsymbol{\tau} \in \mathbb{R}^3$ denoting the total moment in the body-fixed frame, the rigid-body dynamics of XPLORER can be written as

$$\begin{aligned} \dot{\boldsymbol{x}} &= \boldsymbol{v} \\ m\dot{\boldsymbol{v}} &= mg\boldsymbol{e}_3 - f\boldsymbol{R}\boldsymbol{e}_3 + \boldsymbol{\delta_f} \end{aligned} \tag{1a}$$

$$\begin{aligned} \dot{\boldsymbol{R}} &= \boldsymbol{R}\hat{\boldsymbol{\Omega}} \\ \boldsymbol{H}\dot{\boldsymbol{\Omega}} - [\boldsymbol{H}\boldsymbol{\Omega}]_\times\boldsymbol{\Omega} &= \boldsymbol{\tau} + \boldsymbol{\delta_\tau} \end{aligned} \tag{1b}$$

where m denotes the mass of the vehicle, and $\boldsymbol{x} \in \mathbb{R}^3$ and $\boldsymbol{v} \in \mathbb{R}^3$ denote the position and translational velocity of the vehicle, respectively. $\boldsymbol{R} \in \mathbb{R}^{3\times3}$ denotes the rotation from the body frame to world frame (i.e $\boldsymbol{R} :=_b^w \boldsymbol{R}$) and $\boldsymbol{\Omega} \in \mathbb{R}^3$ denotes the angular velocity of the system. Furthermore, $\boldsymbol{e_3} = [0\ 0\ 1]^T$ denotes the z-axis of the inertial frame. The terms $\boldsymbol{\delta_f} \in \mathbb{R}^3$ and $\boldsymbol{\delta_\tau} \in \mathbb{R}^3$ denote the lumped external forces and torques respectively applied on the system. The *hat map* $\hat{\cdot} : \mathbb{R}^3 \to \mathsf{SO(3)}$ is a symmetric matrix operator defined by the condition that $\hat{\boldsymbol{x}}\boldsymbol{y} = \boldsymbol{x} \times \boldsymbol{y}\ \forall\ \boldsymbol{x}, \boldsymbol{y} \in \mathbb{R}^3$ and $[.]_\times$ is the skew symmetric cross product matrix. The rest of the nomenclature is given in Table 1.
Assumption 1. The inertia of the system, $\boldsymbol{H}$ is constant.
Remark 1. The arm angle deviations for the collision tests and flight tests conducted induced a change of about 10^o which produces small inertia deflections, to which the employed P-PID structure of the low-level controller is inherently robust. This implies that the control torques for roll and pitch are not significantly affected, however, the control allocation which converts the desired control torques to the individual motor thrust commands based on the geometry of the chassis is affected. This will affect the performance in the case when the deflection is too high such that symmetricity of the chassis is lost. However, the two case scenarios that we studied are (i) high impact collide and rebound. In this case, there is high deflection (such as $> 10^o$), but this deflection occurs only for a short time due to spring action. The vehicle doesn't destabilize due to the ability of the torsion spring to take the significantly high impact forces. (ii) low-impact collisions which induce deflections $\leq 10^o$. In this case, the symmetry of the vehicle is not significantly affected and the individual motor thrusts are generated by assuming geometric symmetry. The modeling uncertainty, while having minimal impacts on the performance of the XPLORER in this paper, can be more rigorously addressed by employing an adaptive controller which adjusts the motor thrusts according to its morphology, as shown in our past work [56].
As stated, a cascaded P-PID control law is employed for both the position and attitude loops of the low-level controller for XPLORER as shown in Fig. 3 with the errors defined on position and quaternion space respectively. We take advantage of the inherent robustness of the P-PID control structure to obtain good tracking performance in the presence of model uncertainties. The design of adaptive robust controllers to account for disturbances and model uncertainties is beyond the scope of this work and is planned in a future study [56].

3 External Force Estimation and Interaction Control

This section describes the novel external wrench estimation algorithm developed and the corresponding interaction admittance controller [27].

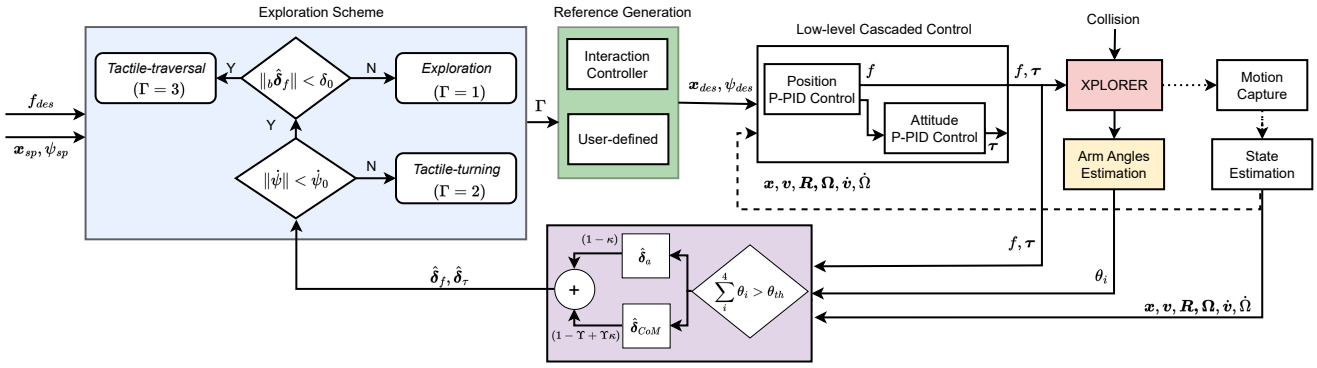

Figure 3: Complete block diagram for an autonomous exploration task with XPLORER. Collisions are characterized by the external wrench shown by the purple shaded block. This value is used to decide the state of exploration (Γ) as shown by the state-machine in the blue shaded block. The value of Γ is then used to generate a suitable reference for position ($\boldsymbol{x}_{des}$) and yaw (ψ_{des}) by either using the interaction controller to reshape the setpoint specified by the user ($\boldsymbol{x}_{sp}$, ψ_{sp}) using f_{des} or bypassing the reshaping process as shown by the two modes in the green colored block. Finally, these references are published to the low-level P-PID tracking controller of the vehicle. The yellow shaded block denotes the arm-angle estimation critical to the proposed external wrench estimation algorithm.

3.1 External Force Estimation

Since the aerial vehicle XPLORER is composed of multiple rigid bodies, we propose a novel force estimator using the estimates from the spring action in addition to those from the center of mass (CoM) to get an improved estimate. By estimating the force applied on each arm, we can estimate the net external force by fusing the acceleration-based methods on the CoM with the estimated force on the arm. The frames used for calculating the force is shown in Fig. 4.

Assumption 2. The external contact force is assumed in a lumped form at any given time.

Remark 2. In this work, we are primarily interested in estimating the net force acting on XPLORER and therefore assume that the external wrench $[\boldsymbol{\delta_f}\ \boldsymbol{\delta_\tau}]^T$ is in a lumped form, as shown in (1a) and (1b). This implies that although we classify whether or not the external force is due to collision by using the deflection of the arm angles, we do not further decouple the external force into the aerodynamic Force and contact Force for the scope of this work.

Assumption 3. The external contact force acts at the origin of the arm frame, normal to the arm plane as shown by $\hat{\delta}_{f_{a_i}}$ in Fig. 4.

Remark 3. The torque generated by this external force can be produced for varying locations of the point of application. However, we estimate the force perpendicular to the arm that generates this torque when applied at the motor location (since this is where the CoM of the arm roughly lies as calculated from SolidWorks) as shown by Fig. 4. Furthermore, we obtain from experiments that the maximum deviation of 78^o occurs for 16N force applied at a distance of 113cm at the motor center. We also notice that there is a maximum of ±5cm error in the possible point of force application on the propeller guards (as shown by δl in Fig. 4). This amounts to a maximum error of 5% for the torque of 1.8080Nm, therefore the assumption can be made.

Assumption 4. The torque estimate is obtained from conventional momentum-based observers from onboard IMUs.

Remark 4. Since we do not directly use the torque information to explore, we only use it to detect a yaw-rate when XPLORER encounters a corner, we choose to employ the momentum-based observers for estimating current torque.

3.1.1 Force Estimate due to Spring Action at Arm

We begin by estimating the external force on each arm using the acceleration-based method. Due to the torsional springs employed at the arm hinge, the arm dynamics can be written as:

$$\mathcal{J}_{zz}\ddot{\theta}_i + b\dot{\theta}_i + k\theta_i = \delta_{\tau_{a_i}} = \delta_{f_{a_i}} l. \tag{2}$$

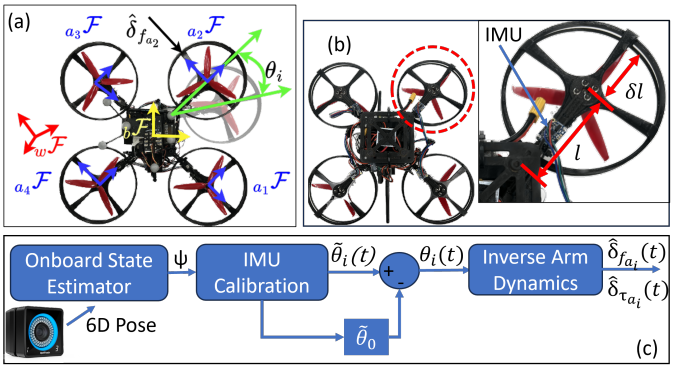

Figure 4: (a) A visualization of the frames used to estimate the net external force on each arm, ${}_{a_2}\hat{\delta}_{f_{a_2}}$. (b) A zoomed-in view to show the placement of IMU and the assumed point of application of $\hat{\delta}_{f_{a_i}}$ (c) Control block diagram to estimate the $\hat{\delta}_{f_{a_i}}$.

where $\mathcal{J}_{zz}$ is the inertia of the arm about the z axis, b and k are the damper and spring coefficients respectively and θ_i is the change in the angle for the i^{th} arm position from its equilibrium. The true external torque is denoted by $\delta_{\tau_{a_i}} \in \mathbb{R}$ and the corresponding normal external force is $\delta_{f_{a_i}} \in \mathbb{R}$. As mentioned in *Assumption 3*, the force is converted to torque by assuming a constant distance l from the motor location to the spring center as shown in Fig. 4. Finally, since the arm angle information is obtained from the IMU, the numerical differentiation of this data can be very noisy. We thus employ a first order low-pass filter to estimate the force on the i^{th} arm by

$$ {}_{a_i}\dot{\hat{\boldsymbol{\delta}}}_{\boldsymbol{f}_{a_i}} = [K_I(\delta_{f_{a_i}} - \hat{\delta}_{f_{a_i}})\ 0]^T \tag{3} $$

where ${}_{a_i}\dot{\hat{\boldsymbol{\delta}}}_{\boldsymbol{f}_a} \in \mathbb{R}^2$ denotes the force obtained in the i^{th} arm frame in the a_1^i and a_2^i directions, K_I denotes the filter gain and the $\delta_{f_{a_i}}$ denotes the true external force.

Now the external force obtained from the i^{th} arm in the inertial frame can be written as $\hat{\boldsymbol{\delta}}^i_{\boldsymbol{f}_a} \in \mathbb{R}^3 = [{}_w\hat{\boldsymbol{\delta}}^{\boldsymbol{i}}_{\boldsymbol{f}_a}\ 0]^T$ with:

$$ {}_w\hat{\boldsymbol{\delta}}^{\boldsymbol{i}}_{\boldsymbol{f}_a} = {}^w_b\boldsymbol{R}\ {}^b_{a_i}\boldsymbol{R}\ \hat{\boldsymbol{\delta}}^i_{\boldsymbol{f}_a} \tag{4} $$

where ${}^w_b\boldsymbol{R}$ denotes the rotation from the body frame to the inertial frame and ${}^b_{a_i}\boldsymbol{R}$ denotes rotation from the arm frame to the body frame as given by (5) below

$$ {}^b_{a_i}\boldsymbol{R} = \begin{bmatrix} \cos\varphi_i & -\sin\varphi_i & 0 \\ \sin\varphi_i & \cos\varphi_i & 0 \\ 0 & 0 & 1 \end{bmatrix} \tag{5} $$

with φ_i being the arm angle deflection for the i^{th} arm calculated as (6)

$$ \varphi_i = \nu_i + \mu_i + \theta_i \tag{6} $$

$\nu_i = \frac{-\pi}{2}$ for $i = 1, 2$ and $\nu_i = \frac{+\pi}{2}$ for $i = 3, 4$ and $\mu_i = \{\frac{3\pi}{4}, \frac{\pi}{4}, \frac{-\pi}{4}, \frac{-3\pi}{4}\}$ for $i = \{1, 2, 3, 4\}$ respectively.

3.1.2 Force Estimate at CoM

Next, following [27], the wrench information at the CoM can also be directly estimated from the acceleration measurement of the vehicle from the high-precision IMU embedded in the onboard flight controller. Rearranging (1a), we obtain

$$ \hat{\boldsymbol{\delta}}_{\boldsymbol{f}_{CoM}} = m\dot{\boldsymbol{v}} - mg\boldsymbol{e}_3 + f\boldsymbol{R} \tag{7} $$

We filter the obtained acceleration to calculate the external force. A median with a low pass filter is used to get a smooth approximation of the acceleration and the control input.

3.1.3 Net Force on XPLORER

The external force obtained at the arm suffers from the limitations of low-pass filtering and fails to estimate the high-frequency peak forces and torques resulting from the collision. Furthermore, if there is no arm deflection from the external force (e.g. when the force is directly applied at CoM), the estimate based on only arm angle feedback doesn't converge to the true force. However, the estimate from the CoM is correct in this case. In order to make the best use of the two approaches and obtain a reliable force estimate, we first define an indicator function to detect whether there is collision and contact on the arms by using the arm deflection as given by (8):

$$\Upsilon = \begin{cases} 1, & \text{if } \sum_{i=1}^{4} |\theta_i| > \theta_{th} \\ 0, & \text{otherwise} \end{cases} \tag{8}$$

where θ_i is the deflection angle of each arm, and θ_{th} is the deflection threshold to detect contact.
We can now estimate the net external force on XPLORER by combining (3) and (7) with an adaptive gain:

$$\hat{\boldsymbol{\delta}}_{\boldsymbol{f}} = \left(1 - \Upsilon + \Upsilon \cdot \boldsymbol{\kappa}_f\right) \cdot \hat{\boldsymbol{\delta}}_{\boldsymbol{f}_{CoM}} + \left(1 - \boldsymbol{\kappa}_f\right) \cdot \Upsilon \cdot \sum_{i=1}^{4} \hat{\boldsymbol{\delta}}^{i}_{\boldsymbol{f}_a} \tag{9}$$

where $\boldsymbol{\kappa}_f \in \mathbb{R}^3 = \xi_f \dot{\hat{\boldsymbol{\delta}}}^{|\cdot|}_{\boldsymbol{f}_{CoM}}$ and $\boldsymbol{\kappa}_\tau \in \mathbb{R}^3 = \xi_\tau \dot{\hat{\boldsymbol{\delta}}}^{|\cdot|}_{\boldsymbol{\tau}_{CoM}}$ are adaptive gains with the tuning parameters ξ_f and ξ_τ. $(\bullet)^{|\cdot|}$ denotes element-wise absolute value of the vector $(\bullet)$. Based on (8) and (9), one gives higher weightage to $\hat{\boldsymbol{\delta}}_{\boldsymbol{f}_{CoM}}$ during collision since the rate of the $\hat{\boldsymbol{\delta}}_{\boldsymbol{f}_{CoM}}$ is higher at the collision instant, so $\boldsymbol{\kappa}_f$ is larger and the peak from CoM-based estimate is retained. On the other hand, when the wrench estimate from the CoM converges slowly the rate of change is near zero at which instant the term $(1-\boldsymbol{\kappa}_f)$ is larger, so the total wrench converges to the arm-based estimation value.

3.2 Interaction Control

In this section, we design an admittance controller that reshapes the reference trajectory and yaw setpoint to maintain a desired force $\boldsymbol{\delta}_{\boldsymbol{f}_{\boldsymbol{des}}}$. The estimated wrench can be used for two different modes depending on what we want XPLORER to perform.

3.2.1 Static-Wrench application

The first mode is that we can employ the external wrench to exert a specific force on the surface and in the second mode, it can be used to steer clear of objects when a contact is detected. For this cases, an admittance controller was designed to maintain a desired interaction force.
To achieve this goal, we employ a standard admittance control strategy [27] and model the desired response as a virtual second-order dynamics:

$$\begin{bmatrix} m_v \boldsymbol{I}_{3\times3} & \boldsymbol{0}_{3\times1} \\ \boldsymbol{0}_{1\times3} & \mathcal{I}_{v,z} \end{bmatrix} \begin{bmatrix} \ddot{\boldsymbol{r}}_d \\ \ddot{\psi}_d \end{bmatrix} + \boldsymbol{D} \begin{bmatrix} \dot{\boldsymbol{r}}_d \\ \dot{\psi}_d \end{bmatrix} + \boldsymbol{K} \begin{bmatrix} \boldsymbol{r}_d - \boldsymbol{r}^*_d \\ \psi_d - \psi^*_d \end{bmatrix} = \begin{bmatrix} \hat{\boldsymbol{\delta}}_f - \boldsymbol{\delta}_{\boldsymbol{f}_{\boldsymbol{des}}} \\ \hat{\delta}_{\tau_{e,z}} \end{bmatrix} \tag{10}$$

where $m_v \in \mathbb{R} > 0$ and $\mathcal{I}_{v,z} \in \mathbb{R} > 0$ are the virtual mass and inertia, $\boldsymbol{r}_d \in \mathbb{R}^3$ and $\psi_d \in \mathbb{R}$ are the reference position and yaw for the low-level controller. $\boldsymbol{D} \in \mathbb{R}^{4\times4} > 0$ and $\boldsymbol{K} \in \mathbb{R}^{4\times4} > 0$ are the diagonal virtual damping and spring gain matrices, respectively. $\boldsymbol{r}^*_d \in \mathbb{R}^3$ and $\psi^*_d \in \mathbb{R}$ are the desired setpoints of position and yaw, respectively which are reshaped according to the external wrench. $\hat{\boldsymbol{\delta}}_{\boldsymbol{f}}$ is the estimated external force, and $\hat{\delta}_{\tau_{e,z}}$ is the current estimated torque about the z-axis (external yaw torque). The complete control block diagram with the interaction controller for XPLORER is shown in Fig. 3.

3.2.2 Disturbance Rejection

In this mode, the UAV is commanded to maintain its intended trajectory in the presence of external disturbances. Towards this the inherent P-PID control structure was exploited for retaining robustness and

it differes from static wrench application since only enough control effort is put to maintain it position and orientation, and a desired force is not being demanded of the UAV.

3.2.3 Yielding to Disturbances

In this flight mode, we leverage a recovery controller that generates a setpoint away from the collision direction to evade any undesired interaction forces and torques. This recovery controller is employed from our previous work [15].

4 Contact-Rich Missions

4.1 Case 1: Contact-based Exploration

This section describes the exploration scheme for XPLORER to explore its surrounding environment. The algorithm uses an explore-and-exploit strategy, taking advantage of the collision-resilient design and the admittance controller to perform tactile-based navigation. This is achieved through a finite state machine shown in Fig. 3, utilizing, $\hat{\boldsymbol{\delta}}_{\boldsymbol{f}} \in \mathbb{R}^3$, representing the force estimate in the inertial frame and yaw rate, $\dot{\psi} \in \mathbb{R}$, as inputs to generate the reference trajectory, $[\boldsymbol{x_{sp}}\ \psi_{sp}]^T$. The exploration strategy is based on well-known coverage planning algorithms using a combination of random walk and wall tracing [57]. However, we employ this exploration scheme for the first time on aerial robots and showcase how it is perfect for exploration with deformable UAVs as opposed to the rigid counterparts due to the added compliance. The workflow of the algorithm is discussed below.
First, the external force needs to be transformed into the body frame using the equation below

$$_{\boldsymbol{b}}\hat{\boldsymbol{\delta}}_{\boldsymbol{f}} = {}^{b}_{w}\boldsymbol{R}\hat{\boldsymbol{\delta}}_{\boldsymbol{f}} \tag{11}$$

where ${}^{b}_{w}\boldsymbol{R}$ denotes the rotation matrix from the inertial frame to the body frame. This information is used to detect and update the contact direction, $\boldsymbol{C_n} \in \mathbb{R}^4$, as a vector of four elements with each element representing the direction in body-frame in which the new contact was made, i.e, in $b_1, -b_1, b_2$ or $-b_2$ directions such that $\|\boldsymbol{C_n}\|_1 = 1$. For example, if $|_{\boldsymbol{b}}\hat{\boldsymbol{\delta}}_{f_x}| > \delta_0$ and $_{\boldsymbol{b}}\hat{\boldsymbol{\delta}}_{f_x} > 0$, C_n is updated to [1,0,0,0]. We also introduce a new variable called the movement direction, λ, which is updated when a new contact is made by using $\boldsymbol{C_n}$. The variable λ takes values from the set {"$+X$", "-X", "$+Y$", "-Y"} to denote which direction to move for the next exploration step in body frame after an object is detected.
The exploration state machine comprises three primary states: *Exploration*, *Tactile-turning* and *Tactile-traversal* corresponding to $\Gamma \in \{1, 2, 3\}$ respectively. Except for *Tactile-turning*, the yaw admittance controller is used to generate yaw setpoints and enable XPLORER to conform to the obstacle's surface. In obstacle-free flight, XPLORER experiences negligible yaw torques and external forces. We choose this as the trigger condition for entering $\Gamma = 1$, i.e. the exploration state. In this state, the vehicle continues to fly forward in space until it encounters an object in its flight path. If $|\dot{\psi}| < \dot{\psi}_0$ and $|_{\boldsymbol{b}}\hat{\boldsymbol{\delta}}_{\boldsymbol{f}_x}|$ or $|_{\boldsymbol{b}}\hat{\boldsymbol{\delta}}_{\boldsymbol{f}_y}| < \delta_0$, XPLORER switches to the *Exploration* state as depicted in Alg. 1 and generates trajectory setpoints along the body x-axis.
At any given time, the state machine continuously checks $\dot{\psi}$ to detect yawing around a point. The yawing can happen when the vehicle is sliding across the edge of an object by exerting a desired force and at the corner it releases the contact. Since the yaw generation is in admittance, this phenomenon causes the yaw rate to peak instantaneously due to the sudden release. Accordingly we check if $|\dot{\psi}| > \dot{\psi}_0$, where $\dot{\psi}_0$ is the threshold for triggering the *Tactile-turning* state shown in Alg. 2. In this state, a controlled yaw is generated at a rate of $\dot{\psi}_c$ in the same direction as XPLORER's yaw until $|_{\boldsymbol{b}}\hat{\boldsymbol{\delta}}_{f_x}|$ or $|_{\boldsymbol{b}}\hat{\boldsymbol{\delta}}_{f_y}| > \delta_{\psi_0}$. δ_{ψ_0} has to be higher than δ_0 because upon switching to *Tactile-traversal* state the $|_{\boldsymbol{b}}\hat{\boldsymbol{\delta}}_{f}|$ should be greater than the δ_0 to register contact and update the contact direction $\boldsymbol{C_n}$. The threshold $\dot{\psi}_0$ is chosen to be high enough such that small yaw rates do not trigger the *Tactile-turning* state. Furthermore, the generated ψ is also limited to 180 degrees to prevent the UAV from yawing indefinitely, in this way UAV will be able to establish contact with the wall again.

Algorithm 1: Exploration

Input: $\dot{\psi}$ & ${}_b\hat{\boldsymbol{\delta}}_{\boldsymbol{f}}$
Output: $[x_{sp_{body}}\ \psi_{sp}]^T$ & Γ

```
if |ψ̇| < ψ̇_o & |_b δ̂_f| < δ_0 then
    X_sp(k) = x + d_step
    Y_sp(k) = Y_sp(k − 1)
    ψ_sp = ψ_des(ψ)
else if |ψ̇| > ψ̇_o then
    Γ = 2
else
    Γ = 3
```

Algorithm 2: Tactile Turning

Input: $\dot{\psi}$ & ${}_b\hat{\boldsymbol{\delta}}_{\boldsymbol{f}}$
Output: $[x_{sp_{body}}\ \psi_{sp}]^T$ & Γ

```
if |ψ̇| > ψ̇_o & |_b δ̂_f| < δ_ψ0 then
    x_sp(k) = x_sp(k − 1)
    if ψ̇ > ψ̇_o then
        ψ_sp(k) = ψ_sp(k − 1) + ψ̇_c dt
    else
        ψ_sp(k) = ψ_sp(k − 1) − ψ̇_c dt
else
    Γ = 3
```

Algorithm 3 illustrates the *Tactile-traversal* state which allows the EXPLORER to traverse obstacles by maintaining contact with the obstacle. XPLORER continues to move in the previous direction λ until δ_0 is reached and $\boldsymbol{C_n}$ is updated when a new contact is made. As mentioned earlier, the elements of $\boldsymbol{C_n}$ are updated by a binary value based on which λ also gets updated as shown in Alg. 3. The new λ is set along the obstacle plane and towards the right-hand side of the current movement direction to ensure consistent performance. The interaction controller is then used to ensure the vehicle maintains contact with the obstacle by exerting a force of f_{des} onto the object while flying forward. In scenarios where XPLORER encounters obstacles in two directions, $\boldsymbol{C_n}$ is updated with the latest collision direction. The setpoints generated by the admittance controller to maintain contact with the obstacle whilst the drone traverses in the perpendicular direction of the obstacle are denoted by $X_{des}(f_{des})$ and $Y_{des}(f_{des})$ in the body frame.

As mentioned, the entire trajectory generation is first computed in the body frame and then transformed into the inertial frame ($[x_{sp}\ y_{sp}\ z_{sp}]^T$) to account for orientation before publishing into the flight controller, as shown in (12)

$$[x_{sp}\ y_{sp}\ z_{sp}]^T = {}^w_b\boldsymbol{R}[X_{sp}\ Y_{sp}\ Z_{sp}]^T \tag{12}$$

where $[X_{sp}\ Y_{sp}\ Z_{sp}]$ denote the setpoints in the body frame. Similarly in Algorithm 1 and 3, $[x\ y\ z]$ denote the current location of XPLORER in the inertial frame.

To ensure the setpoints are within d_{step}, i.e. the frontier region of the current position of the vehicle, the setpoints are bounded. Also, the setpoint for the z-axis is kept constant since this work focuses on exploring the 2D space. The exploration of the entire 3D space is beyond the scope of this study.

4.2 Case 2: Contact-based Mapping

The ability to explore the environment by maintaining contact can be used to generate a map of the obstacle. This synthesized map can be used for motion planning by XPLORER or other autonomous robots. The overview of the contact-based mapping framework is depicted in Alg. 4. The algorithm utilizes the ${}_b\hat{\boldsymbol{\delta}}_{\boldsymbol{f}}$, the CAD model of XPLORER, and the global pose to generate the obstacle boundary map. We use the Open3D library [58] for processing the point cloud generated.

Obstacle map generation initializes when $|{}_b\hat{\boldsymbol{\delta}}_{\boldsymbol{f}}| \geq \delta_{map}$. δ_{map} is taken to be slightly higher than f_{des}. This choice is to ensure mapping is conducted only when there is firm contact with the obstacle. As an additional condition, the mapping starts if the UAV is flying. The contact normal, $\boldsymbol{C_n}$, provides the direction of the obstacle, in which an object of dimension 0.25 m × 0.08m × 0.5 m is added to the point

Algorithm 3: Tactile Traversal

Input: $\dot{\psi}$ & ${}_b\hat{\boldsymbol{\delta}}_{\boldsymbol{f}}$
Output: $[x_{sp_{body}}\ \psi_{sp}]^T$ & Γ

Function `CollisionNormal()`:
  if λ = "$+X$" *or* "$-X$" **then**
    if ${}_b\hat{\delta}_{f_x} > \delta_{0x}$ **then**
      $\boldsymbol{C_n} = [1,0,0,0]$
    else if ${}_b\hat{\delta}_{f_x} < -\delta_{0x}$ **then**
      $\boldsymbol{C_n} = [0,1,0,0]$
  else if λ = "$+Y$" *or* "$-Y$" **then**
    if ${}_b\hat{\delta}_{f_y} > \delta_{0y}$ **then**
      $\boldsymbol{C_n} = [0,0,1,0]$
    else if ${}_b\hat{\delta}_{f_y} < -\delta_{0y}$ **then**
      $\boldsymbol{C_n} = [0,0,0,1]$
  return $\boldsymbol{C_n}$
Function `MoveDirection()`:
  $\boldsymbol{C_n} \leftarrow$ ContactNormal()
  if $\boldsymbol{C_n} == [1,0,0,0]$ **then**
    λ = "$+Y$"
  else if $\boldsymbol{C_n} == [0,1,0,0]$ **then**
    λ = "$-Y$"
  else if $\boldsymbol{C_n} == [0,0,1,0]$ **then**
    λ = "$-X$"
  else if $\boldsymbol{C_n} == [0,0,0,1]$ **then**
    λ = "$+X$"
  return λ
Function `TrajectoryGeneration()`:
  $\lambda \leftarrow$ MoveDirection()
  $\psi_{sp} = \psi_{des}(\psi)$
  if λ = "$+X$" **then**
    $X_{sp}(k) = x + d_{step}$
    $Y_{sp}(k) = Y_{des}(f_{des})$
  else if λ = "$-X$" **then**
    $X_{sp}(k) = x - d_{step}$
    $Y_{sp}(k) = Y_{des}(f_{des})$
  else if λ = "$+Y$" **then**
    $X_{sp}(k) = X_{des}(f_{des})$
    $Y_{sp}(k) = y + d_{step}$
  else if λ = "$-Y$" **then**
    $X_{sp}(k) = X_{des}(f_{des})$
    $Y_{sp}(k) = y - d_{step}$
Function `Main()`:
  CollisionNormal()
  MoveDirection()
  TrajectoryGeneration()

Algorithm 4: Mapping Framework

Input: $[x,y,z]^T$, ψ , ${}_b\hat{\boldsymbol{\delta}}_f$, $\boldsymbol{C_n}$ & λ
Output: *Point Cloud Data*

if $|{}_b\hat{\boldsymbol{\delta}}_{\boldsymbol{f}}| \geq \delta_{map}$ **then**
  if $\lambda_{prev} \neq \lambda$ **then**
    Add Corner Block to Point Cloud
  else
    Add Obstacle to Point Cloud in $\boldsymbol{C_n}$ axis
else
  Store Point Cloud Data

cloud, offset by 0.21 m from the position of XPLORER. The offset corresponds to the perpendicular distance from XPLORER's center to the edge of each side. In corner cases where the move direction, λ, is not the same as the previous move direction, a constant block is added diagonally with an offset of 0.417 m to the point cloud to make it continuous around the corners (shown in Supplementary Video 3). The point cloud is generated at 30 Hz to obtain a high-resolution map of the obstacle. The map is stored as a Polygon File Format (PLY) as per the ASCII format, and it consists of the location of each point in the point cloud. For this scope of the work the map generation was done on a computer with AMD Ryzen 5 CPU with 16 Gigabytes of RAM, the DDS middle-ware used in ROS2 enabled offloading the computation from the high-level companion computer to a powerful computer on the same network. The map generation primarily relies on the pose of the UAV, which is currently obtained using the motion capture system. Onboard sensing such as visual-inertial odometry or IMUs can be explored to obtain the pose of the vehicle, but they may introduce inaccuracies due to noise and saturation as a result of the impact. In this paper, we employ a motion capture system to obtain the UAV's pose.

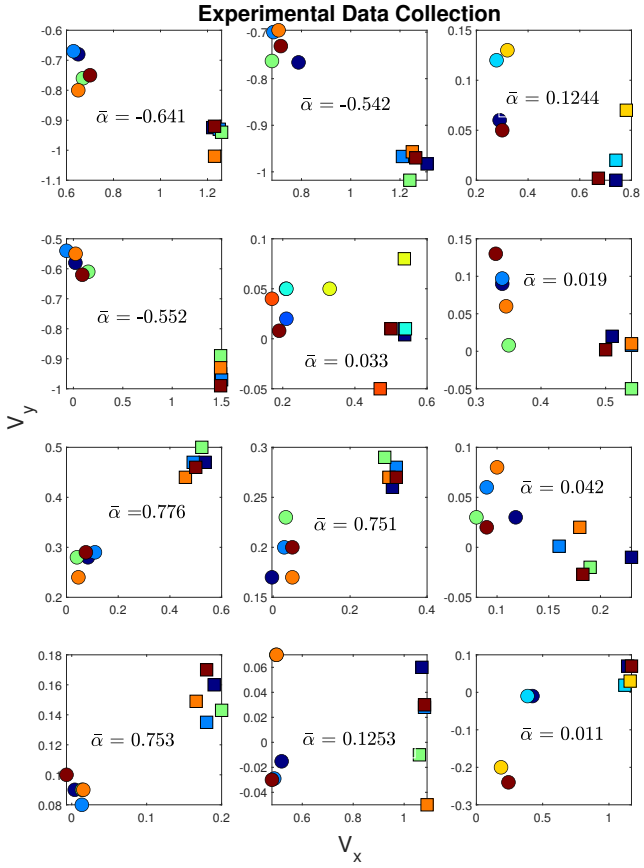

Figure 5: Experimental data for post collision velocity inference and motivation for collide-to-brake maneuver. The x-axis denotes the x direction velocity and y-axis denotes the y direction velocity. The square markers show the pre-collision velocities and the circular markers represent the corresponding post-collision ones for each color, respectively.

4.3 Case 3: Collide-to-Brake Maneuvers

In this section, we present a novel application of collision resilient quadrotors for decelerating and obtaining a sudden change in momentum. Towards this we collect collision data at different angles and develop a neural network that predicts the post collision velocity. With this information, new trajectories are available with collision-inclusive flights by leveraging state jumps from conventional hybrid control theory such as in [59].

Towards understanding post-collision behavior, a set of 60 flight experiments was performed to generate a collision model for XPLORER in various collision scenarios as shown in Fig. 5. The yielding to disturbance mode and the corresponding recovery controller from Section 3.23 was employed. The Fig. 5, This

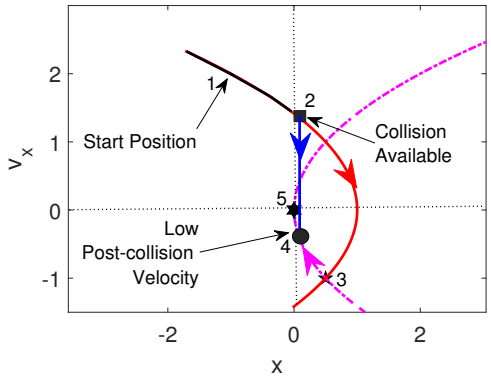

Figure 6: Simulation results to describe the idea of collide-to-decelerate maneuvers for obtaining minimum-time trajectories by exploiting collisions.

plot denotes how pre-collision velocities map to the post-collision velocities in various scenarios. Various pre-collision states corresponding to x and y velocities are chosen as different case scenarios. Five trials are conducted for each case scenario. Furthermore, $\bar{\alpha}$ represents the mean heading direction to the collision surface of all trials corresponding to a specific case. From the figure, it is seen that for al large number of high pre-collision velocities, the post-collision velocities are low. For example in subplots (1,1), (1,2) and (2,1) the magnitude of pre-collision velocities is 1m/s however, the post-collision velocities are near 0.5m/s in magnitude. This motivates us to exploit braking maneuvers by using collisions. A neural network was fit to predict the post collision velocity for a given pre collision velocity and angle of incidence.

With this information, we can now envision how collisions are beneficial by enabling the state-jumps. We explain this concept via an example and related simulations. Consider the phase portrait for a one dimensional vehicle as shown in Fig. 6. The vehicle is flying with some velocity from point 1 and at point 2, there is a collision available. If the vehicle chooses to collide, there is sudden decrease in post collision velocity and drops to point 4 from where it can then decelerate to reach point 5 i.e equilibrium. If this was not the case, the vehicle would fly and brake at point 3 according to the bang-bang optimal control law for achieving minimum time flights. Therefore, the minimum time for both these maneuvers can be calculated by using the neural network prediction and tools from hybrid control theory [59]. If a collision is ideal, this should be chosen to perform fastest waypoint navigation.

We show via experiments that by exploiting maneuvers where the UAV collides and loses almost all kinetic energy presents novel collide-to-brake maneuvers which compliant UAVs can demonstrate efficiently. Therefore, to achieve the minimum time trajectory, we choose the maximum velocity that XPLORER can physically attain and demonstrate collide-to-stop maneuvers for reaching to goal in minimum-time as discussed in the results section.

5 Results and Discussion

In this section, we first describe the system setup for data collection and the related data processing. Next, we present the experimental results for each analytical derivation as presented above. All our code is available at `https://github.com/ASU-RISE-Lab`.

5.1 Experimental Setup

XPLORER's chassis hosts the flight controller, power module, and high level controller, as seen in Fig. 7a. Flight controller utilized is a PIXHAWK flight controller with the Intel UP Board as the companion computer. The high-level companion computer is used to relay the position and orientation data from the indoor motion capture system to the flight controller at 120 Hz. A 4S lithium polymer battery of 3300 mAh LiPo battery of 14.8V, 50C is used for the power supply. The motors are controlled utilizing

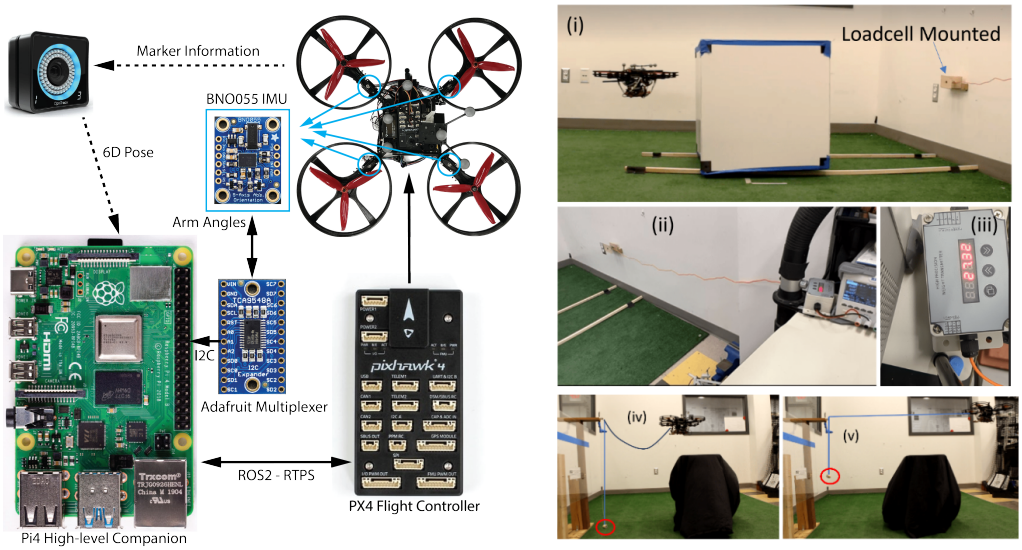

Figure 7: (a) The complete electronics overview for autonomous missions with XPLORER. IMUs (BNO055) are used to obtain the proprioceptive information about XPLORER's arm angles. A motion capture system is used to obtain the localization information and a Raspberry Pi4 is employed as the the high-level companion computer. (b) (i)-(iii) The setup for validating the external force applied by the UAV on a static object. The setup consists of a loadcell with a digital reader (calibrated to show Decinewtons, dN) which measures the force applied when the UAV is pushing it. The admittance controller is employed to maintain a desired constant force on the wall by using the external wrench estimate. (iv)-(v) A pulley experiment was designed to lift a mass of 150gms using the UAV XPLORER and a string tied near the CoM. This experiment was carried out to validate the wrench estimation without the presence of contacts, so there is no angle deformation.

Lumenier 30A BLHeli_S Electronic Speed Controllers (ESCs) and the entire system has a mass of 1.12 kg. The BNO055 IMU sensors are connected to the high-level companion computer which is the Raspberry Pi4B via a Adafruit multiplexer and serial connection.

5.1.1 Inputs for arm and CoM-based wrench estimates

We employ low-cost off-the-shelf inertial measurement units (IMUs) on each arm to measure acceleration and estimate the external force on the arm. IMUs were employed due to their low costs, lightweight, strong resilience, and easy integration, compared to other sensors such as encoders.. Accordingly, four 9-DOF IMUs (BNO055, Adafruit, New York, NY) are mounted on XPLORER (one on each arm) and are connected to the RaspberryPI via serial communication at 50 Hz. The Euler angles are computed using the Adafruit BNO055 library. A median low-pass with a band-stop filter is employed to obtain accurate estimates of the arm angles, θ_i, at any given instant. For the system identification, the inertia about z-axis for the arm, $\mathcal{J}_{zz}$ was calculated using SolidWorks to be 0.0015kgm^2. We design an experiment where the base of the XPLORER is held by a clamp and the torsional spring-based arm is first loaded to a certain fixed position using a force sensor. Then it is released and the motion capture system is used to generate the trajectory of the arm. We then use the MATLAB System ID toolbox to obtain the b and k values as 0.009 and 1.307 for $\mathcal{J}_{zz} = 0.0015\text{kg}m^2$ in (3). Finally the estimated force and net torque values $\hat{\boldsymbol{\delta}}_a^i$ are computed as discussed in Section 3.1.
For the CoM-based estimate we use the normalized thrust and torques generated from the onboard flight controller PIXHAWK from the cascaded P-PID attitude and position controller. The normalized thrust value is scaled by 32.5 units, which is obtained empirically by calculating the hover trust, and used to calculate the approximate value of the actual thrust.

Table 2: Parameters & Thresholds used in Experiments

Symbol	Threshold Value
$\dot{\psi}_0$	0.4 rad/s
$\dot{\psi}_c$	0.26 rad/s
δ_0	1.5 N
δ_{ψ_0}	1.6 N
d_{step}	0.25 m
f_{des}	1.25 N
δ_{map}	1.51 N

5.1.2 Localization information

All the experiments are conducted in an indoor test facility at ASU using a 10-camera motion capture system (OptiTrack, NaturalPoint Inc, OR) for obtaining the localization data and 3D pose estimation of XPLORER. The Root Mean Square Error (RMSE) for the localization data is ±5 cm. As mentioned in Section 2.1, we use a ROS2-RTPS bridge to establish the communication between the high-level companion computer and the low-level flight controller. For every experiment presented, we run at least three trials to validate the reliability and thoroughness of our proposed methods and obtain consistent performance for every trial. To make the article more organized, we chose to show the results of only one trial from all the experiments.

5.1.3 Environment setup

To validate the performance of the algorithms, XPLORER was tested in two distinct environments containing obstacles. In the first scenario, a rectangular object measuring 1.22 m × 1.0 m was set up using acrylic panels, as illustrated in Fig. 10aa. The use of transparent acrylic panels helped in tracking XPLORER's movement through the obstacle via the motion capture system. This setup was designed to evaluate the exploration algorithm's ability to navigate 90-degree turns and map the entire boundary of the obstacle to obtain its dimensions. The second scenario, depicted in Fig. 10a(b), featured a corridor with slanted walls containing both concave and convex edges. This scenario effectively tests the algorithm's ability to navigate through complex environments.

5.2 External Force and Interaction Control

In this section, we present the results for the external wrench estimation algorithm and the designed interaction controller in Section 3.2 for three experimental studies: (i) for a static wall wrench application where we also present the validation data (ii) the second for a box-pushing experiment to validate the performance of the interaction controller (iii) validation with a rigid UAV for the box-pushing interaction task.
In order to calculate the wrench at the CoM, the controller's normalized force and torque values are obtained from the onboard flight controller. As discussed before, the force value is scaled by a factor of 32.5 to generate the required thrust. Due to the constant nature of the scaling factor for the thrust value, the effect of the battery on the motor thrust is not accounted for. This method can be significantly improved by performing a PWM-thrust mapping curve using RPM sensors on the motor. However, this is beyond the scope of this work. The gains for the interaction controller in (10) are set to

$$\boldsymbol{D} = \begin{bmatrix} 24.5 & 0 & 0 & 0 \\ 0 & 24.5 & 0 & 0 \\ 0 & 0 & 0 & 0 \\ 0 & 0 & 0 & 1 \end{bmatrix}, \boldsymbol{K} = \begin{bmatrix} 24.5 & 0 & 0 & 0 \\ 0 & 24.5 & 0 & 0 \\ 0 & 0 & 0 & 0 \\ 0 & 0 & 0 & 1 \end{bmatrix}$$

with $m_v = \mathcal{I}_{v,z} = 1$. These values are obtained by multiple trials of experiments to obtain the desired response of compliance.

5.2.1 Static wrench application

The results for a static wrench application task are shown in Fig. 8(a)-(b). The reference for this experiment is set to $\boldsymbol{\delta f}_{ref} = [-1\ 0\ 0]^T$ for applying a 1 N force on the wall.
In order to validate the force estimates obtained from our proposed method, we use a load cell (ATO Micro 5kg Tension and Compression Load Cell, S Type, ATO, Diamond Bar, CA) mounted on the wall as shown in Fig. 7b(i-iii). A digital reader is attached to the load cell which is calibrated to display the force readings when the load cell is compressed. The UAV takes off and starts applying the force on the box whose other end pushes the load cell. The sampling rate of the sensor is 20 Hz, hence it is noted that the force values settles to its set desired force value. A video of the experimental setup is available in Supplementary Video 7.
The insets in Figs. 8a shows the deviation of the arm angles used to calculate the arm wrench ${}_w\hat{\boldsymbol{\delta}}_{f_{a_i}}$. The dotted magenta line shows the actual force measured by a force sensor set up on the wall. It is seen that the estimate from the CoM shown by the blue dotted line takes time to converge, however, the arm angle-based force estimate converged to the set desired force sooner without the collision peak. By fusing both methods, the proposed estimator retains the peak from the CoM-based method and also converges faster. For this experiment, the true force applied on the wall after settling was measured to be approximately 1.3 N using a force sensor as shown by the dashed magenta line, demonstrating an accuracy of 0.3N for this task.
A similar experiment for $\boldsymbol{\delta f_{des}} = [-2\ 0\ 0]^T$ was conducted and the results are shown in Fig. 8c. The true force on the wall was measured to be 2.42 N. For over 3 trials the true force was approximately 0.42 N more than the estimated force during constant application. This error could be due to the unmodeled dynamics, imperfect sensor measurements, and coupling between external and aerodynamic wrenches.
We also validate the force applied by the UAV when there is no deformation of the arm angle and only CoM estimate is present. Towards this goal, we tie a 150-gram mass to one end of a pulley system and command the UAV XPLORER to hover at a set location which allows the mass to hang in air. This entire setup in shown in Fig. 7b(iv-v). Ideally, the force experienced by the UAV XPLORER should be equal to $mg = 1.47$ N. For this experiment the CoM converged to 1.8 N. This error can be attributed to the discrepancies of the location of the UAV which may result in additional forces in other directions and can also stem from errors in assumption on the model used for converting normalized control thrust to the actual force. The validation results for only the CoM-based estimate are presented in Fig. 8d. The setup consists of the UAV pulling a mass of 150 gms via a pulley system. Ideally, at equilibrium conditions, the net force exerted by the XPLORER to lift the mass is 1.47 N. From 5 trials, we see that the estimated wrench converges to 1.8 N. This error can arise from the inaccurate location of the UAV during the free flight and friction from the pulley system.
The error in the proposed estimator can stem from the assumptions on the point of application of force and the force mapping from the thrusts, which is a function of the battery health and is currently assumed as a constant scaling value. Even with these assumptions, the results show that without any additional high-end force-torque sensors and payload addition, the proposed acceleration-based adaptive estimator gives reliable wrench estimation results to support autonomous contact-rich tasks.

5.2.2 Box-pushing experiment

For the box pushing experiment, $\boldsymbol{\delta f}_{ref} = [-2\ 0\ 0]^T$ to push a box with 2 N by overcoming the friction on the carpet. The results are shown in Fig. 9a, we see that there is a loss in contact as shown by the arrow, which is attributed to the unaccounted slippage and the non-linear friction during experiments. However, this slippage is minor such that at least 1.5 N is continuously applied upon the box. However, a similar experiment conducted with a rigid quadrotor shows deteriorated performance due to the inability of the rigid chassis to make smooth and continuous contact without the spring action. These comparison plots are shown in Fig. 9b. We further demonstrate the safe-interaction policy in real-life in the Supplementary Video 1 for disturbance rejection, demonstrating compliant behavior for safe human-

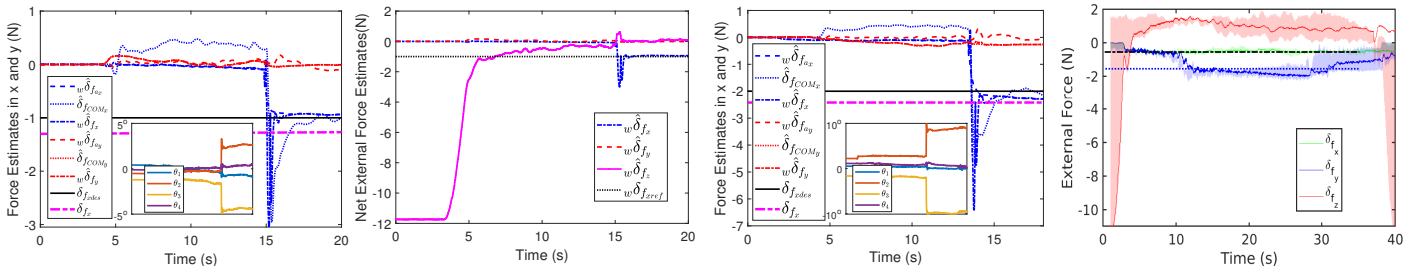

(a) (b) (c) (d)

Figure 8: Results for the force estimation and interaction controller. (a-b) show the results for a static force application task where XPLORER is commanded to apply a 1 N force on a wall. (a) shows the individual estimates and validation using CoM method, arm angle deviations, and the proposed method in inertial x and y axes. The inset shows the corresponding deviation in arm angles. (b) shows the net external force estimated in all directions. (c) shows the results of a similar experiment but $\delta_{f_{ref}} = 2N$. (d) shows the validation results for a constant force applied at CoM to verify the performance using the estimates from the CoM only. All the results are thoroughly described in Section 5.2.

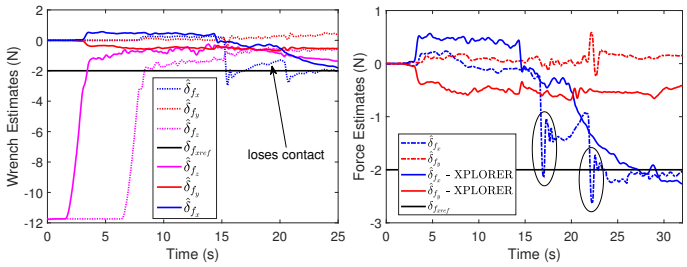

(a) (b)

Figure 9: A box-pushing experiment conducted with the XPLORER. (a) shows the results for XPLORER in two cases. For the case with dotted data, initially, when contact is made, there is some loss in contact as shown by the arrow. This was, however, one of the few cases when it loses contact. For multiple other trials, the XPLORER gradually applies force and maintains contact as shown by the increasing value of $\hat{\delta}_{f_x}$ (solid lines) (b) Comparison with a rigid UAV's performance. The rigid UAV loses contact (dotted blue line) as opposed to the smooth contact by XPLORER shown by the blue solid line.

aerial interaction and for the push-the-box scenario. Please note that we refer to disturbance rejection as the flight mode when the interaction controller is not activated and compliant control for the case when the desired force is set to zero in the interaction controller. For the disturbance rejection, we observed that due to the deformable chassis, XPLORER returns to the setpoint without overshoot, unlike its rigid counterparts where the disturbance leads to an increase in kinetic energies, thereby providing superior performance when compared to rigid conventional vehicles.

5.3 Contact-based Exploration

The exploratory algorithm proposed in Section 4.1 is validated by real-time implementation on XPLORER.

5.3.1 Input data

The state machine in Fig. 3 requires clean input to function appropriately, so it is necessary to filter the external force estimate, $\hat{\boldsymbol{\delta}}_{\boldsymbol{f}}$, and yaw rate, $\dot{\psi}$. To that end, a moving average filter with 50 samples is employed to filter ${}_b\hat{\boldsymbol{\delta}}_{\boldsymbol{f}}$, while a low-pass filter is utilized to eliminate noise in the yaw rate, $\dot{\psi}$.

5.3.2 Parameters

The state machine for XPLORER relies on several parameters that require fine-tuning through trials. After extensive testing, we have determined the optimal values for these parameters that work well in all environments, and they are listed in Table 2. To prevent excessive force on the objects in the environment and considering flight time, we limited δ_0 to 1.5 N, though it is capable of exerting forces greater than 2 N. Furthermore, as XPLORER approaches right-angled corners/edges and rotates around those

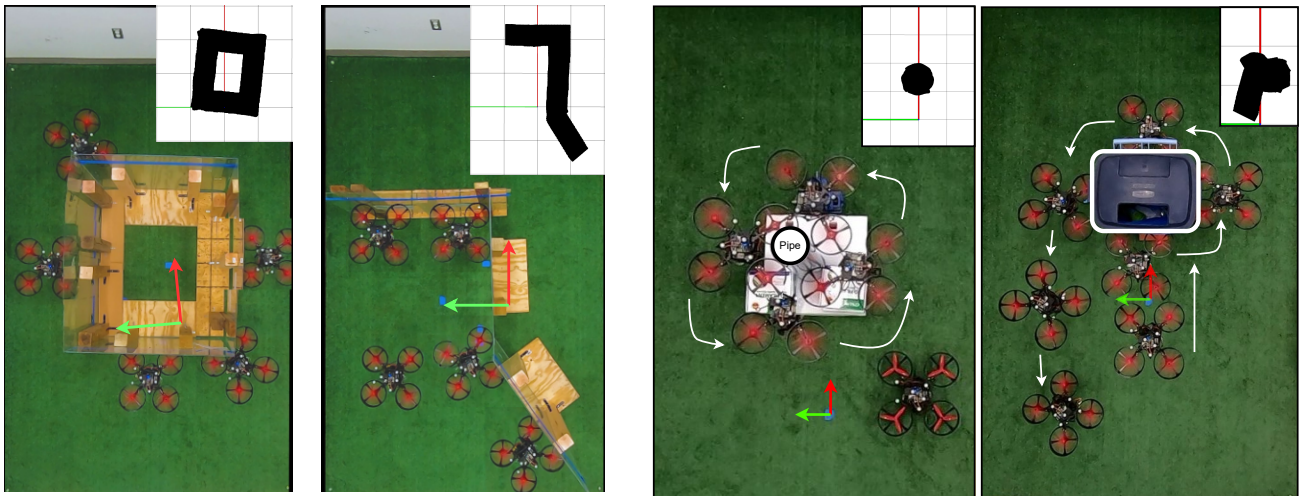

(a) (b)

Figure 10: (a) Top view of the experimental setups with the generated maps and overlaid images of XPLORER throughout the experiment. Left: Environment with a closed box-like structure. Right: An environment with concave and convex edges, representing a wall-like structure. (b) Left: Environment with an acrylic pipe as an obstacle. Right: An environment with a trash can as an obstacle. Please note that the results for these experiments are shown in the Fig. 11.

points, the corresponding yaw rate is measured to be 0.6 rad/s, which correlates to the force of 1.5 N being applied. Any increase in the applied force will result in a higher yaw rate. We choose 0.4 rad/s to detect such a maneuver. For the *Tactile-turning* state, the controlled yaw maneuver is performed at 0.26 rad/s.

5.3.3 Results for XPLORER

XPLORER takes off and upon reaching a hover height of 0.7 m, it switches to *Exploration* state and moves in the positive x direction in the body frame. Once it detects the threshold external wrench, δ_0 in its movement direction, it switches to the *Tactile-traversal* state as described in Section 4.1. It maintains contact with the obstacle by applying f_{des} force and moves across the environment. Throughout the flight, the yaw is in admittance ensuring two arms of the UAV are in contact with the obstacle. In this experiment the *Exploration* and *Tactile-traversal* states are predominantly used for the navigation as shown in Fig. 11a and is shown in Supplementary Video 2.

5.3.4 Results for a Rigid UAV

In this section, we present results for exploration experiments with a rigid quadrotor of the same dimensions. The same exploration scheme developed for XPLORER was offloaded to a rigid quadrotor to check the performance for exploration. We conducted both wall-traversal and the box-traversal experiments out of which only the wall-traversal succeeded with the rigid quadrotor.
For the wall traversal results shown in Fig. 12a, the rigid UAV takes off and upon making initial contact, applies the desired force on the wall and initiates the *Tactile-traversal*. When it detects the second wall, it engages the traversal motion in the body y direction as shown by the black line.
For the second case scenario, which involves a box-like structure, the aim is to also engage the *Tactile-turning* state to go around corners. As shown in the Fig. 12b, after initial contact and desired force application, the state machine moves to *Tactile-turning* upon detecting a high yaw-rate. However, due to the absence of the spring-damper action, during this turning, significant oscillations are observed in yaw and the UAV was not able to maintain contact and apply desired force during turning, thereby unable to move to the tactile-traversal state again. The same observations are made in all four experiments conducted for this case. As a result, the exploration for a rigid drone failed in all four trials conducted for a box-like exploration. Finally, another unpredictable behavior was observed with the rigid UAV, as shown

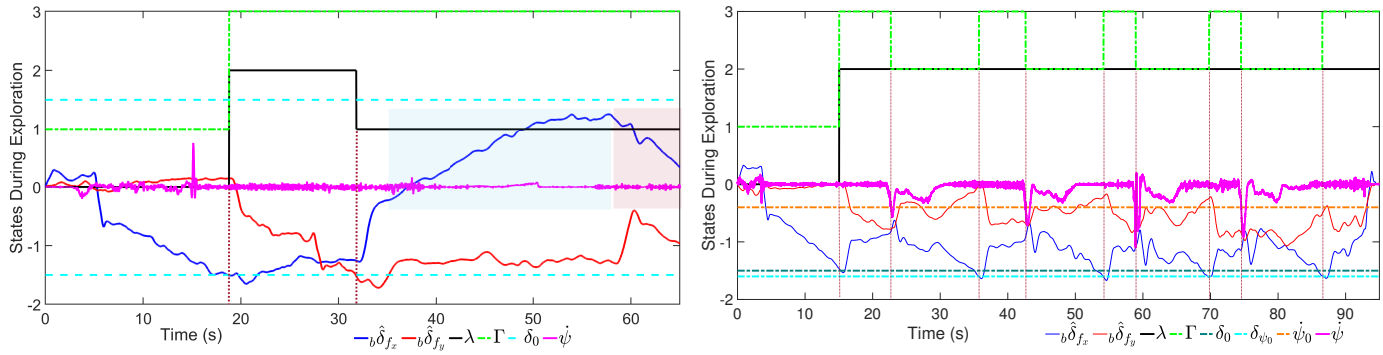

(a) Wall traversal (b) Box traversal

Figure 11: Exploration results for two case scenarios. (a) shows the results for the exploration of a wall-like structure. The exploration states are triggered when the threshold for δ_0 is crossed. In this case, only two states corresponding to Γ =1 and 3 are activated. The blue and red regions show that even during moving in state Γ = 3, there is an external wrench observed in the $\pm$ x direction indicating the presence of unmodeled frictional and wall-effects (b) shows the results for exploration of a box-like structure. The exploration states are switched when the thresholds for δ_0 or $\dot{\psi}_0$ are crossed. In this case, all three states corresponding to Γ = 1, 2, 3 are activated. For both plots, the vertical dotted lines show the time-instants where the thresholds are crossed to trigger the state-machine for deciding the exploration state. Units for the quantities are as follows: yawrate, $\dot{\psi}$, and yawrate threshold $\dot{\psi}_0$ are in rad/s, the wrenches ${}_b\hat{\delta}_{f_x}$ and ${}_b\hat{\delta}_{f_y}$ are in N, with non-dimensional values of λ and Γ. Please note: the top view of the experiments (a) and (b) are shown in Fig.10a.

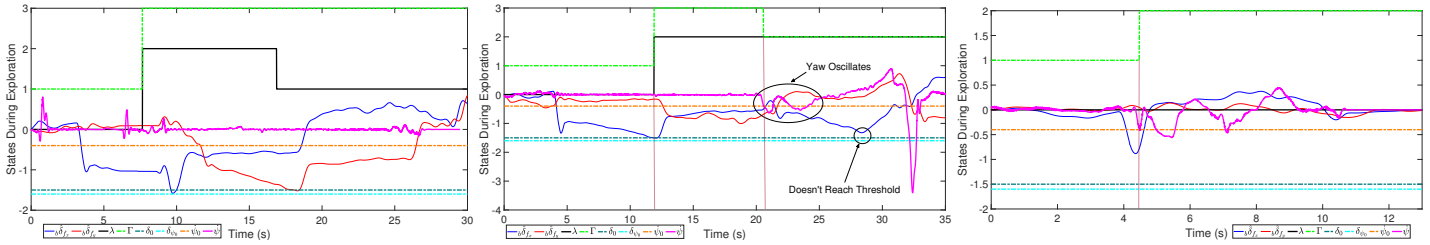

(a) Wall traversal (b) Box traversal (c) Failure Case

Figure 12: Exploration results for three case scenarios for rigid UAV. (a) shows the results for the exploration of a wall-like structure. The rigid UAV performs as desired, and the exploration states Γ = 1, 3 are duly activated. (b) shows the results for the exploration of a box-like structure, which shows the performance for convex corners. The rigid UAV tries to yaw, however, due to the high interaction force required for maintaining the turning maneuver and absence of compliance in the chassis brings about oscillatory yaw motion, failing to engage *Tactile-traversal* after *Tactile-turning*. (c) shows the results for cases when the force and torque at initial contact is so high, such that the yaw torque leads to engaging the *Tactile-turning* state with Γ = 2 and fails to start the exploration with Γ = 3 that is *Tactile-traversal*.

in Fig. 12c. Sometimes whenever the rigid UAV makes an impact, due to the high rebound velocities, and the presence of yaw admittance control given by (10), there is a high yaw-rate which falsely triggers the *Tactile-turning* and the entire exploration fails. However, this behavior is not observed with the XPLORER due to the damping effect and shock-absorbing nature of the torsion spring in the arm. The results of this experiment are shown in Supplementary Video 6.

5.4 Mapping

In the previous experiment, XPLORER successfully demonstrated its capability to navigate the boundary wall setup. Here, we demonstrate that it can perform loop closure, i.e., circumnavigate an obstacle and generate a complete map. This application enables the extraction of the obstacle's dimensions and its position in the environment, as detailed in Section 4.2.

5.4.1 Parameters

To perform mapping of the obstacle, an additional parameter δ_{map} is introduced. It is set slightly higher than f_{des} at 1.51 N to ensure that the mapping is initiated only when the vehicle has firm contact with the obstacle. Furthermore, an additional check is added to ensure that mapping is conducted only when

XPLORER is flying. The other parameters used during this process can be found in Table 2.

5.4.2 Results

First the exploration algorithm described in the above section is initiated. Upon reaching a hover height of 0.7 m, XPLORER switches to *Exploration* state and moves in the positive x direction in the body frame. Upon encountering the wall, it proceeds to move across the obstacle until it reaches the corner where it releases and yaws. This triggers the *Tactile-turning* state which allows it to yaw in a controlled manner and establish contact with the adjacent wall, effectively switching back to the *Tactile-traversal* state. It continues traversing all the edges until it returns to the initial contact position, thereby achieving loop closure. From Fig. 11b we can infer that all three states corresponding to $\Gamma = 1$, 2, and 3 are activated whilst circumnavigating the obstacle. The generated map allows for the measurement of the dimension of the box, which is 1.231 m × 1.019 m and the actual dimensions are 1.22 m × 1.0 m. The accuracy is about 96.72% for computing the area of the box. One source of the mapping error is the imperfect position estimation (small errors from the motion capture system in our experiment), as it propagates in state estimation and to the point cloud data. The results are also shown in Supplementary Video 3.
Furthermore, the map of the environment as generated by the proposed algorithm is shown in the insets of Fig. 10a(a) and (b) for the box-like structure and wall-boundary traversal respectively. Additional experiments were conducted for exploration and mapping of rounded objects and objects with gaps/with slots in them as described in Supplementary Information.

5.5 Collide-to-brake

In this subsection, we experimentally demonstrate how collisions can be exploited to perform improved tracking and minimum time waypoint navigation with XPLORER. Towards this, we employ a reduced 1D collision model for which the coefficient of restitution was nearly 0.09 as identified from the network, thereby demonstrating almost perfect inelastic collisions.
The rise time (τ_r) and the settling time (τ_s) are chosen as the metrics to evaluate the performance of collide-to-brake (CoB) maneuver for XPLORER for all cases. The results for the conventional, collision-exclusive trajectory is shown in Fig. 13a. In this case, the vehicle first reaches the setpoint, overshoots and then tries to minimize the error by slowly converging to the reference. The τ_r and τ_s are noted to be 2.27 and 8.995 seconds, respectively. Furthermore, over three trials the RMSE error was around ± 3cm for this case. For collision-inclusive trajectories, the experimental results show that XPLORER reaches the wall with maximum velocity and the e is low enough in order to stop the vehicle at the wall itself by absorbing the collision energies. This demonstrates the collide-to-stop maneuver. Consequently, the vehicle stops near the wall almost instantaneously as shown by the plots in Fig. 13b. The τ_r and τ_s are calculated to be 1.046 and 5.292 seconds, respectively which are faster than the conventional trajectories. For the case where the vehicle performs collide-to-decelerate and regulates itself to a setpoint beyond the wall, and results in Fig. 13c show significantly shorter convergence time with τ_r = 1.685 seconds and τ_s = 3.631 seconds, respectively. The low settling time for the later case as compared to a sudden stop at the wall can be attributed to the wall effect which affects the performance of the vehicle for the collide-to-stop case as also noted in Section 5.2. We also noted that the RMSE values over 6 trials for the collision-inclusive trajectories were ± 0.5cm showing improved tracking accuracy than the conventional maneuvers. This can be attributed to the dissipation of kinetic energies upon collision, leading to improved decelerating performance. All the experimental results for CoB are shown in Supplementary Video 4.

6 Conclusion

In this section we summarize the current contributions of the article and discuss some interesting areas which are still open for future research.

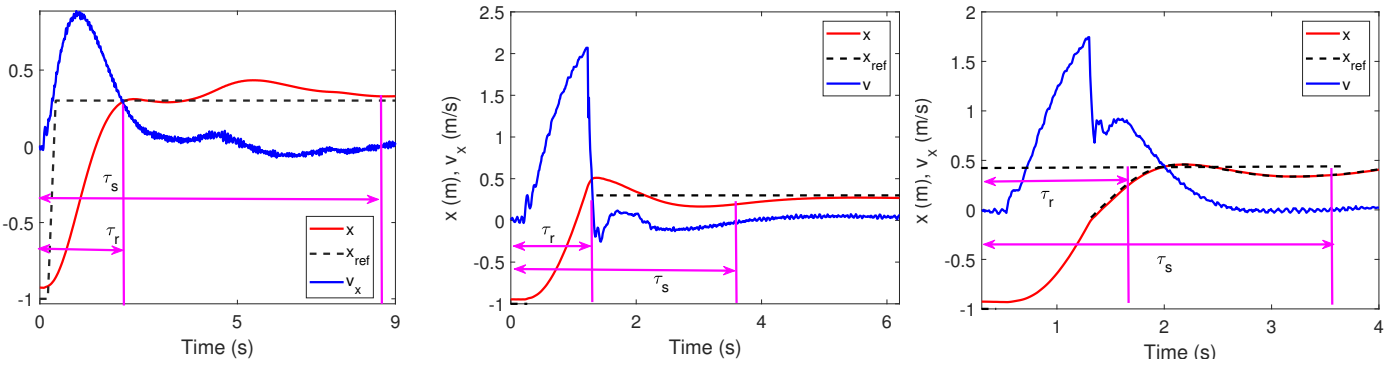

(a) Without collision (b) Collide-to-stop (c) Collide-to-decelerate

Figure 13: Results for CoB applied on XPLORER. (a) Simulation results and the phase-portrait for the proposed collision-inclusive arcs with state-jumps. The blue-blue-green-black states depict the minimum-time trajectories as compared to the conventional red-black curve as obtained from bang-bang control law without collisions. (b) Experimental results for a case without collision, with $\tau_r = 2.27$ and $\tau_s = 8.995$ seconds. (c) Experimental results for the collide-to-stop maneuver, $\tau_r = 1.046$ and $\tau_s = 5.292$ seconds (d) Experimental results for the case collide-to-decelerate, $\tau_r = 1.685$ and $\tau_s = 3.631$ seconds.

6.1 Summary

In this work we presented a complete autonomous planning and control framework for a passive deformable quadrotor, XPLORER, to perform physical interaction tasks, including exploring unknown environments through contact, generating maps, and planning minimum-time and collision-inclusive trajectories. As the first step, the acceleration-based wrench estimation algorithm was modified to account for the change in morphology to get accurate wrench estimates. The wrench estimation algorithm was verified by experiments for a static wrench application and a pushing experiment. Furthermore, a novel exploration and mapping scheme was presented which adaptively switched between the various available flight modes to explore an unknown flight space. This algorithm was successfully implemented and validated to generate a map of the space for a wall-like object and a box-like object. Finally, a novel collision-inclusive trajectory planner, CoB, was introduced which generated minimum-time paths by considering the state jumps introduced by collisions. With the information of the map generated in the previous step, this planner can successfully generate minimum-time paths, even faster than those obtained from classical bang-bang control laws without leveraging collisions. The results showed that CoB successfully generated minimum time paths which was 40.38% faster than the conventional trajectory tracking methods. Furthermore, due to the dissipation of the kinetic energies after the collision, the deceleration was faster and the tracking performance was significantly improved.

6.2 Limitations and Future Work

Given the comprehensive framework for exploration, mapping, and navigation, there is still room for improvement from the low-level and wrench estimation perspectives. Future work will look into collision isolation for the exact wrench estimate on the arm and model individually the various external wrenches instead of the lumped model assumption. This is particularly beneficial since, in our current algorithm, we do not model wall-effects which cause XPLORER to get stuck near corners and increase in friction during the *Tactile-traversal* modes. In such scenarios, a viscous drag model for friction also fails and significant aerodynamic studies have to be conducted to study this phenomena. Our current proposed methodology is limited to applications to flat surfaces. Future work shall look into developing an exploration algorithm for non-flat and tilted surfaces to improve the range of applications for such compliant UAVs.

The current mapping framework relies entirely on localization data obtained from the motion-capture system, exploring the implementation of onboard sensors and state estimation techniques will enable the vehicle to be deployed in actual environments. The sensor fusion approach can be considered for the mapping framework, making it possible to fuse the generated tactile-based map with those produced by LiDAR or vision systems.

For the collision-inclusive trajectory planner, we demonstrated how collisions can be harnessed on top of a shortest-path generator to obtain minimal-time flights. Potential future work can extend the local time-optimal trajectory planner. However, a few important aspects which are specific to the XPLORER design and influence the post collision states are described below when considering 2D time-optimal control. The compliant UAV employed for physical interaction in this article, XPLORER, can absorb energy so the rebound is not strong. Hence extending the formulation to 2D for angled collisions is not beneficial since instead of change in momentum, this UAV absorbs energy and loses momentum even at high velocities for all angles of collisions. Finally, modeling of 2D post collision states can be challenging and requires detailed attention to many factors in the experimental design. For example, the geometry of the surface and contact surface material properties need exhaustive experiments and analysis for modeling post collision states. The collision model is also influenced by the recovery controllers, since a UAV is open-loop unstable system and a reference should always be generated. Depending on how this reference is generated after collision, the post collision dynamics vary. This requires a large number of experiments to cover different angles and approach velocities with different recovery controllers.
All of the future work will make robots ready to embrace and potentially benefit from collisions in real-world applications such as infrastructure inspection, search and rescue, and environmental monitoring.

Acknowledgements
The authors would like thank to Bill Nguyen for helping in designing filters for the arm angle estimation.

References

[1] M. R. Freeman, M. M. Kashani, P. J. Vardanega, *Journal of Unmanned Vehicle Systems* **2021**, *9*, 2 75.

[2] F. Ruggiero, V. Lippiello, A. Ollero, *IEEE Robotics and Automation Letters* **2018**, *3*, 3 1957.

[3] D. Hausamann, W. Zirnig, G. Schreier, P. Strobl, *Aircraft Engineering and Aerospace Technology* **2005**, *77*, 5 352.

[4] S. Mishra, D. F. Syed, M. Ploughe, W. Zhang, *IEEE/ASME Transactions on Mechatronics* **2021**, *26*, 4 1914.

[5] S. Kim, S. Choi, H. J. Kim, In *2013 IEEE/RSJ International Conference on Intelligent Robots and Systems*. IEEE, **2013** 4990–4995.

[6] A. Suarez, G. Heredia, A. Ollero, In *2015 IEEE/RSJ International Conference on Intelligent Robots and Systems*. IEEE, **2015** 1627–1632.

[7] M. Kovac, *Science* **2016**, *352*, 6288 895.

[8] S. Mintchev, D. Floreano, *IEEE Robotics & Automation Magazine* **2016**, *23*, 3 42.

[9] K. Patnaik, W. Zhang, *International Journal of Intelligent Robotics and Applications* **2021**, *5*, 3 365.

[10] D. Falanga, K. Kleber, S. Mintchev, D. Floreano, D. Scaramuzza, *IEEE Robotics and Automation Letters* **2019**, *4*, 2 209.

[11] N. Meiri, D. Zarrouk, In *2019 International Conference on Robotics and Automation*. IEEE, **2019** 5302–5308.

[12] N. Bucki, J. Tang, M. W. Mueller, *IEEE Transactions on Robotics* **2022**.

[13] K. Patnaik, S. Mishra, S. M. R. Sorkhabadi, W. Zhang, In *2020 IEEE/RSJ International Conference on Intelligent Robots and Systems*. IEEE, **2020** 1364–1370.

[14] Z. Liu, K. Karydis, In *2021 IEEE International Conference on Robotics and Automation*. IEEE, **2021** 183–189.

[15] K. Patnaik, S. Mishra, Z. Chase, W. Zhang, In *2021 IEEE/ASME International Conference on Advanced Intelligent Mechatronics*. **2021** 418–423.

[16] P. H. Nguyen, K. Patnaik, S. Mishra, P. Polygerinos, W. Zhang, *Soft Robotics* **2023**.

[17] S. Haddadin, *Towards safe robots: approaching Asimov's 1st law*, volume 90, Springer, **2013**.

[18] A. De Luca, R. Mattone, In *Proceedings of the 2005 IEEE international conference on robotics and automation*. IEEE, **2005** 999–1004.

[19] B. Yüksel, C. Secchi, H. H. Bülthoff, A. Franchi, In *2014 IEEE/ASME international conference on advanced intelligent mechatronics*. IEEE, **2014** 433–440.

[20] M. Orsag, C. Korpela, P. Oh, S. Bogdan, A. Ollero, *Aerial manipulation*, Springer, **2018**.

[21] V. Serbezov, H. Panayotov, M. Todorov, S. Penchev, *IOP Conference Series: Materials Science and Engineering* **2020**, *878*, 1 012039.

[22] A. Ollero, G. Heredia, A. Franchi, G. Antonelli, K. Kondak, A. Sanfeliu, A. Viguria, J. R. Martinez-de Dios, F. Pierri, J. Cortés, et al., *IEEE Robotics & Automation Magazine* **2018**, *25*, 4 12.

[23] F. Ruggiero, J. Cacace, H. Sadeghian, V. Lippiello, In *2014 IEEE international conference on robotics and automation*. IEEE, **2014** 2093–2099.

[24] F. Ruggiero, J. Cacace, H. Sadeghian, V. Lippiello, *Robotics and Autonomous Systems* **2015**, *72* 139.

[25] M. Ryll, G. Muscio, F. Pierri, E. Cataldi, G. Antonelli, F. Caccavale, D. Bicego, A. Franchi, *The International Journal of Robotics Research* **2019**, *38*, 9 1045.

[26] C. D. McKinnon, A. P. Schoellig, In *2016 IEEE/RSJ International Conference on Intelligent Robots and Systems*. IEEE, **2016** 5651–5657.

[27] T. Tomić, C. Ott, S. Haddadin, *IEEE Transactions on Robotics* **2017**, *33*, 6 1467.

[28] P. Pfändler, K. Bodie, U. Angst, R. Siegwart, In *SMAR 2019-Fifth Conference on Smart Monitoring, Assessment and Rehabilitation of Civil Structures-Program*. SMAR, **2019** We–4.

[29] J. Hu, S. Zhang, E. Chen, W. Li, *Construction and Building Materials* **2022**, *325* 126718.

[30] K. Alexis, G. Darivianakis, M. Burri, R. Siegwart, *Autonomous Robots* **2016**, *40* 631.

[31] K. Bodie, M. Brunner, M. Pantic, S. Walser, P. Pfändler, U. Angst, R. Siegwart, J. Nieto, *IEEE Transactions on Robotics* **2020**, *37*, 3 709.

[32] M. Tognon, H. A. T. Chávez, E. Gasparin, Q. Sablé, D. Bicego, A. Mallet, M. Lany, G. Santi, B. Revaz, J. Cortés, et al., *IEEE Robotics and Automation Letters* **2019**, *4*, 2 1846.

[33] G. Nava, Q. Sablé, M. Tognon, D. Pucci, A. Franchi, *IEEE Robotics and Automation Letters* **2019**, *5*, 2 331.

[34] B. Brogliato, B. Brogliato, *Nonsmooth mechanics*, volume 3, Springer, **1999**.

[35] J.-C. Zufferey, A. Beyeler, D. Floreano, *Flying Insects and Robots* **2010**, 73–86.

[36] D. Schafroth, S. Bouabdallah, C. Bermes, R. Siegwart, *Journal of Intelligent and Robotic Systems* **2009**, *54* 245.

[37] R. He, A. Bachrach, N. Roy, In *2010 IEEE International Conference on Robotics and Automation*. IEEE, **2010** 1–8.

[38] S. Shen, N. Michael, V. Kumar, In *2011 IEEE International Conference on Robotics and Automation*. IEEE, **2011** 20–25.

[39] D. Scaramuzza, M. C. Achtelik, L. Doitsidis, F. Friedrich, E. Kosmatopoulos, A. Martinelli, M. W. Achtelik, M. Chli, S. Chatzichristofis, L. Kneip, et al., *IEEE Robotics & Automation Magazine* **2014**, *21*, 3 26.

[40] A. Briod, P. Kornatowski, A. Klaptocz, A. Garnier, M. Pagnamenta, J.-C. Zufferey, D. Floreano, In *2013 IEEE/RSJ International Conference on Intelligent Robots and Systems*. IEEE, **2013** 3987–3992.

[41] P. De Petris, H. Nguyen, M. Kulkarni, F. Mascarich, K. Alexis, In *2021 IEEE International Conference on Robotics and Automation*. IEEE, **2021** 2286–2292.

[42] T. Lew, T. Emmei, D. D. Fan, T. Bartlett, A. Santamaria-Navarro, R. Thakker, A.-a. Aghamohammadi, In *Robotics Research: The 19th International Symposium ISRR*. Springer, **2022** 938–958.

[43] N. Khedekar, F. Mascarich, C. Papachristos, T. Dang, K. Alexis, In *2019 International Conference on Robotics and Automation*. IEEE, **2019** 4161–4167.

[44] L. M. Gonzalez de Santos, E. Frias Nores, J. Martinez Sanchez, H. Gonzalez Jorge, *Sensors* **2021**, *21*, 2 642.

[45] J. Zha, M. W. Mueller, In *2021 IEEE International Conference on Robotics and Automation*. IEEE, **2021** 7943–7949.

[46] J. L. Schonberger, J.-M. Frahm, In *Proceedings of the IEEE Conference on Computer Vision and pattern recognition*. **2016** 4104–4113.

[47] W. Zhen, Y. Hu, H. Yu, S. Scherer, In *2020 IEEE International Conference on Robotics and Automation*. IEEE, **2020** 6773–6779.

[48] A. J. Davison, In *Computer Vision, IEEE International Conference on*, volume 3. IEEE Computer Society, **2003** 1403–1403.

[49] R. Mur-Artal, J. M. M. Montiel, J. D. Tardos, *IEEE Transactions on Robotics* **2015**, *31*, 5 1147.

[50] J. Zhang, S. Singh, *Robotics: Science and Systems* **2014**, *2*, 9 1.

[51] D. Cattaneo, M. Vaghi, A. L. Ballardini, S. Fontana, D. G. Sorrenti, W. Burgard, In *2019 IEEE intelligent transportation systems conference*. IEEE, **2019** 1283–1289.

[52] P. De Petris, S. J. Carlson, C. Papachristos, K. Alexis, *arXiv preprint arXiv:2212.03196* **2022**.

[53] S. Mintchev, S. de Rivaz, D. Floreano, *IEEE Robotics and Automation Letters* **2017**, *2*, 3 1248.

[54] P. H. Nguyen, K. Patnaik, S. Mishra, P. Polygerinos, W. Zhang, *Soft Robotics* **2023**.

[55] A. Fabris, E. Aucone, S. Mintchev, *Advanced Intelligent Systems* **2022**, *4*, 11 2200113.

[56] K. Patnaik, W. Zhang, *IEEE Control Systems Letters* **2023**.

[57] K. M. Hasan, K. J. Reza, et al., In *2014 International Conference on Informatics, Electronics & Vision (ICIEV)*. IEEE, **2014** 1–6.

[58] Q.-Y. Zhou, J. Park, V. Koltun, *arXiv:1801.09847* **2018**.

[59] A. Cristofaro, C. Possieri, M. Sassano, In *2019 IEEE 58th Conference on Decision and Control*. IEEE, **2019** 6301–6306.